Thin Solid Films 696 (2020) 137779

Contents lists available at ScienceDirect

Thin Solid Films

journal homepage: www.elsevier.com/locate/tsf

Comprehensive analysis of blue diode laser-annealing of amorphous silicon films

Minok Park[a], Zacharias Vangelatos[a], Yoonsoo Rho[a], H.K. Park[b], Jin Jang[c], Costas P Grigoropoulos[a,*]

[a] Laser Thermal Laboratory, Department of Mechanical Engineering, University of California at Berkeley, Berkeley, CA 94720-1740, USA
[b] Laser Prismatics LLC, PO Box 24803, San Jose, CA, 95154, USA
[c] Advanced Display Research Center, Department of Information Display, Kyung Hee University, Seoul 130-701, South Korea

ARTICLE INFO

Keywords:
Low temperature polycrystalline silicon (LTPS)
Blue diode laser
Silicon thin film
Lateral grain growth
Glass deformation

ABSTRACT

The low temperature polycrystalline silicon (LTPS) method has proved to be a technical breakthrough, accomplishing semiconductor thin films with remarkable mobility for a range of high-performance displays, including liquid crystal display and organic light emitting diodes. However, utilizing a conventional excimer laser source for LTPS incurs high cost. In this paper, we demonstrate a comprehensive analysis of the crystallization mechanism of a-Si film (94 nm) and the thermal deformation of the glass substrate induced by Blue diode Laser Annealing (BLA). BLA provides high quality laterally grown crystals over 4 μm × 10 μm on glass substrates, which were examined by optical microscopy, scanning electron microscopy, and Raman spectroscopy. In addition, the permanent deformation introduced by the annealing process is numerically modeled, instantiating how to control the heat conduction from the thin film that affects the substrate. Our findings reveal that the permanent thermal deformation depth that can be obtained is comparable to the roughness of the silicon film for the optimum scanning speed and laser power. The combination of both experimental and numerical results elucidates the manifested physical mechanisms during the BLA process and provides the guidelines to improve the experimental parameters of this process.

Submitted on *Thin Solid Films* on August 7, 2019, Final version submitted on December 16, 2019.

1. Introduction

The low temperature polycrystalline silicon (LTPS) technology has been established as the predominant technique for a plethora of thin film transistor electronic applications, such as liquid crystal display and organic light emitting diode. To facilitate fabricating these components, excimer laser has been employed to efficiently induce crystallization of a-Si thin films and enhance the mobility of Si thin film by transforming it into polycrystalline silicon (p-Si) thin film [1,2]. Nevertheless, the excimer laser technology has been forestalled by the manufacturing cost of electronic devices due to its prodigal cost, the maintenance of its components, its typically low wall-plug efficiency (~ 1%) and the cost of the gas mixtures. There have been attempts to replace the excimer laser with light sources, such as the diode-pumped solid state green laser [3], the frequency-doubled YAG laser [4], and the Ar^+ laser [5]. Even though LTPS can be achieved utilizing these sources, resulting in poly-Si with large grain size over 10 μm, their limitation in scalability and efficiency still obstructs the commercialization of electronic devices on even larger substrates (i.e. above Gen10 (2.88 × 3.13 m) substrate).

However, the blue diode laser, with wavelength at the visible spectrum (440 nm), has captured the attention of the researchers as an industrial LTPS processing tool due to its scalability, low-cost, exceptional optical power density, small form factors, and high wall-plug efficiency (~ 30%) [6,7,8,9,10,11]. More specifically, its optical penetration depth at 22 nm for the aforementioned wavelength is deeper than the penetration depth corresponding to UV excimer laser wavelengths. To put these values into perspective, the optical penetration depth of the excimer laser, at wavelength 308 nm, is 6 nm, which is significantly lower than that of the blue diode laser. In addition, considering the time scale offered by the continuous wave mode, the heating mode is volumetric, providing advantages to produce larger lateral crystal grains, greater than 10 μm, along the scanning direction rather than through the depth of the material. Nevertheless, the large thermal diffusion length (~ 1 μm at dwelling time equal to 1 μs), associated with heating beyond the glass transition temperature, can

* Corresponding author.
E-mail address: cgrigoro@berkeley.edu (C.P. Grigoropoulos).

https://doi.org/10.1016/j.tsf.2019.137779
Received 14 August 2019; Received in revised form 16 December 2019; Accepted 27 December 2019
Available online 28 December 2019
0040-6090/

cause texturing of the glass substrate, despite the existence of thermal buffer layers, such as SiO_x and SiN_x between a-Si film and the substrate, which bounds the defect-free and uniform device fabrication. Moreover, it has not been demonstrated how the thermal effects influence the grain growth from the scope of a numerical model.

To surpass these barriers, we demonstrate an analysis of the blue diode laser annealing (BLA) process, investigating the a-Si crystallization mechanism due to the BLA-induced thermal effect on the glass substrate to further advocate the industrial feasibility of this technique. To comprehend the crystallization mechanism, the temperature fields of Si films are solved numerically utilizing a finite difference method to compare the experimental results. In addition, Secco-etched optical microscopy and scanning electron microscopy revealed that over 4 μm × 10 μm grown crystals can be fabricated along the scanning direction. Hundreds of nanometers sized grains can also be obtained, adjacent outside this directional solidification zone. The low deviation of Raman shift of p-Si thin film from that of single crystal silicon wafer elucidates the high quality of crystallinity with low residual stress inside the film. The temperature fields of the buffer layer, consisting of plasma-enhanced chemical vapor deposition (PECVD) SiO_2, and the glass substrate are numerically solved. Finally, the deformation profiles of the glass substrate are calculated with finite element analysis and validated by interferometry. Hence, by optimizing the scanning speed, the permanent deformation of the glass substrate can be mitigated to be comparable to the roughness of the p-Si film. This methodology will provide a coherent framework to comprehend how the thermo-mechanical effects affect the BLA process.

2. Experiments & simulations

2.1. Experiments and methods

As a standard optical set-up, a single blue diode laser beam controlled by a power controller is transferred through the optics delineated in **Fig. 1A** to the sample, and an elliptically focused beam shape is formed, shown in **Fig. 1B**. During the experimental procedure, the length of the short axis is required to be miniscule to decrease the annealing duration τ ($\tau = \frac{\text{Short axis}}{\text{Scanning velocity}}$). However, the length of the long axis is enlarged to increase the overall crystallization area. Therefore, two convex lenses with 10X microscope objective lens (Mitutoyo, NA 0.28) are installed, while their corresponding distances, L_1, L_2, and L_3 depicted in **Fig. 1A**. These lengths are adjustable to enable the variance of the size of the focused laser beam. A cylindrical lens is installed in the middle of the optical beam path to enlarge the length of long axis only, while the length of the short axis is preserved constant. The focused blue laser has a long axis and a short axis approximately equal to 290 μm and 28.5 μm respectively, as it is illustrated in **Fig. 1B**, based on the $1/e^2$ beam diameter. For the laser processing, the a-Si thin film (94 nm) is placed on a variable scanning speed translator. White light is illuminated with a 5X objective lens (Mitutoyo, NA 0.14) from the backside of the sample. The lens is connected to a charge coupled device (CCD) camera in order to monitor the crystallization of a-Si film in-situ.

In order to prepare the sample, an a-Si:H film (substrate temperature: 360 °C, power: 30 W, and SiH_4, H_2, and He at 2.0 torr) is deposited by PECVD after deposition of 400 nm thick SiO_2 buffer layer on glass substrate. Afterwards, the a-Si:H film is dehydrogenated at 450 °C, such that the hydrogen content in a-Si film is less than 1%. The thickness of a-Si film (94 nm) is measured by an ellipsometry after the dehydrogenation.

By a single scanning of optical power 4.61 W ± 0.2 W and scanning speed 75 mm/s, three different regimes are formed [12]. Therefore, hereafter they will be classified for detailed interpretation as follows: zone 1 (fine grained Si), zone 2 (hundreds of nm sized crystals), and zone 3 (directional crystal growth regime), presented in **Fig. 1B**. The fabricated size of zone 3 is 200 μm, and the total featured size from the end to the end is 346 μm under the above conditions.

In order to study the grain boundary of p-Si thin film after the annealing process, commercially available Secco etchant (Transene Company INC) consisting of a mixture of $K_2Cr_2O_7$, HF, and H_2O [13] is employed. The etchant is diluted with DI water by the ratio of 4 (DI water: Secco etchant = 4: 1). Next, the p-Si sample is dipped into it for 20 s. Finally, 10: 1 buffered hydrofluoric is used to remove the oxide layer formed during etching process.

2.2. Numerical simulations

To analyze the crystallization of a-Si thin film and the heat flux to the glass substrate, the 3-dimensional heat conduction equation incorporating phase change from solid to liquid is solved utilizing the finite difference method [14]. Taking into account that the optical penetration depth is 22 nm at 440 nm wavelength and the a-Si film (< 100 nm) is much thinner compared to the thermal diffusion length, which is approximately 20 μm at dwelling time 380 μs and scanning speed 75 mm/s, it is presumed that at this time scale the dominating mechanism across the entire film is volumetric heating. Hence, the system was modeled as a simplified 2-dimensional layer for the a-Si layer. However, the PECVD SiO_2 layer and the glass substrate are modeled as three dimensional [14]. The numerical simulation was performed only for the melting phase change of silicon from a-Si to ʟ-Si, to characterize the melting of a-Si and the transient temperature of liquid Si (l-Si), while the modeling of re-solidification mechanism from ʟ-Si to p-Si was not included. To apply the real laser profile for the simulation, a knife-edge experiment was performed with the laser beam spatial profile fitted with Gaussian functions. The mechanical and thermal properties of the a-Si and ʟ-Si have been reported elsewhere [15,16,17], and the optical properties (n = 5.10, and k = 1.47 at 440 nm) of a-Si were measured with spectroscopic Ellipsometry (J.A.

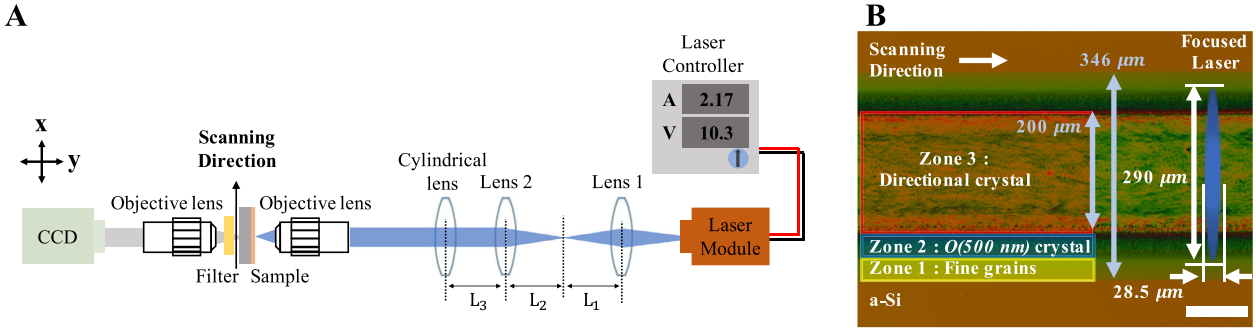

Fig. 1. Blue diode laser annealing process (A) optical set up of the BLA system, (B) three different zones fabricated by BLA; zone 1 (fine grained regime), zone 2 (hundreds of nm sized crystals), and zone 3 (directional crystals). The length of zone 3 is 200 μm, and the total length of the zones is 346 μm. An elliptically focused laser profile is utilized (colored blue). The length of short axis is 28.5 μm and that of long axis is 290 μm based on e^2 beam diameter. Scale bar is 100 μm.

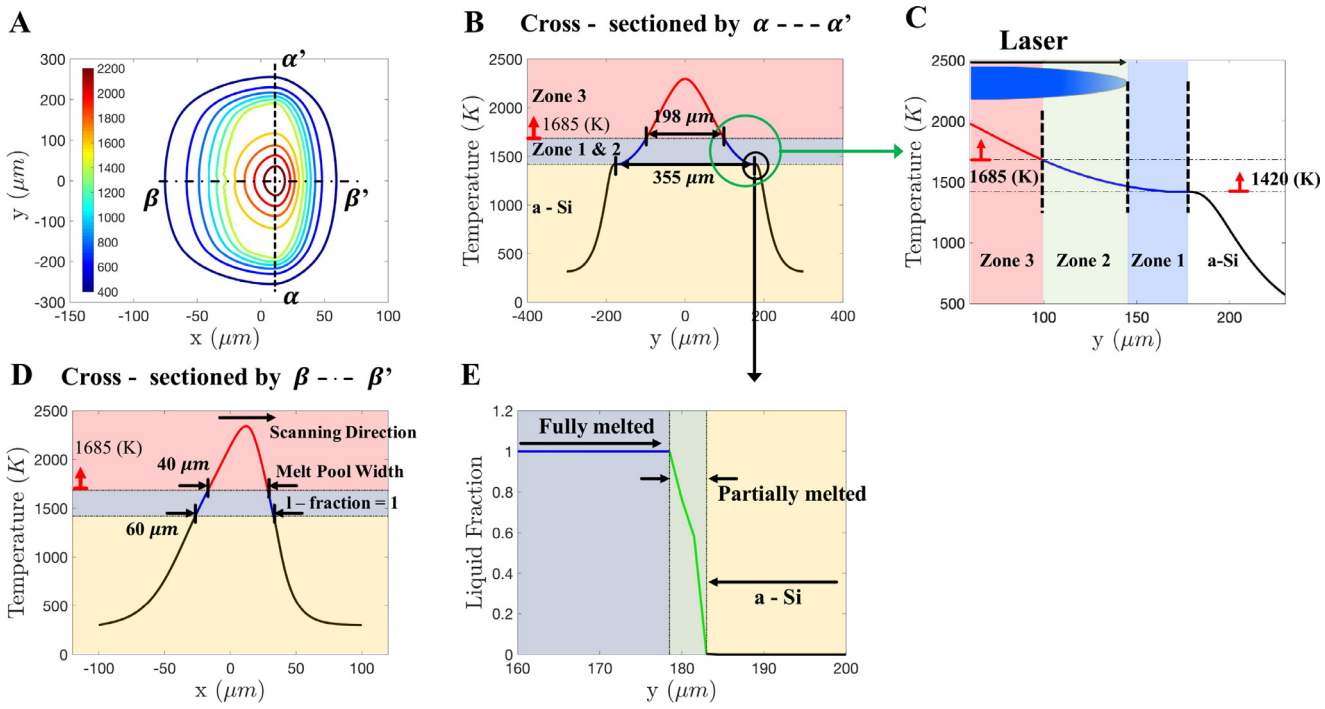

Fig. 2. Simulation results of the temperature field (A) Transient isotherms of silicon film for the laser irradiation conditions of 4.61 W at 75 mm/s, (B) and (D) are cross-sectional temperature fields for $\alpha - \alpha'$, and $\beta - \beta'$, respectively. (C) magnified temperature field normal to the scanning direction in (B). There is a liquid fraction between the fully melted and a-Si regime in (B), which is shown in (E). It is expected for the fully melted region to be 355 μm, and for partially melted region to be 5 μm. + $\boldsymbol{x}$ is scanning direction.

Woollam). As the properties of PECVD SiO_2 film with 400 nm thickness converge to the properties of the bulk SiO_2 [18], those of the SiO_2 interlayer and the glass substrate were selected from literature [19].

For laser power equal to 4.61 W and scanning speed 75 mm/s, the calculated transient silicon temperature-field is presented in Fig. 2**A**. The crucial factor for the development of directionally grown crystals is superheating above the equilibrium melting point of silicon (1685 K) combined with a slow cooling rate [5]. Thus, the heated regime was set above 1685 K along the scanning direction as a melting pool width, depicted in Fig. 2**D**. Regarding the temperature profile normal to the scanning direction shown in Fig. 2**B**, the length of the region heated over 1685 K is expected to be 198 μm and the calculated length of fully melted Si (i.e., liquid fraction becomes 1) is 355 μm, which is consonant with the fabricated length of zone 3 (200 μm) and the total featured length (346 μm) presented in Fig. 1**B**. These simulation results will be juxtaposed with the experimental results in Fig. 3 and Fig. 4 and discussed in the next section.

In addition, to study the effects of the laser power and scanning speed to the permanent deformation of the glass substrate, coupled thermal simulations with static structural analysis was performed, utilizing finite element analysis in ANSYS. The properties of the glass that are required to perform the simulations are the density $\rho = 2500$ kg/m^3, the coefficient of thermal expansion $9 \times 10^{-6} K^{-1}$, the Young's modulus $E = 73{,}000$ MPa, the Poisson's ration $\nu = 0.27$, the thermal conductivity $k = 1.4$ W/mK and the tensile yield strength $\sigma_Y = 248$ MPa. In addition, as there is disparity in the temperature, the thermal expansion coefficient was dependent on the temperature, as this has been reported elsewhere [20].

To calculate the deformation field, the heat flux profile obtained by the thermal simulations is applied to the surface of the substrate. The thermal analysis simulations provide the temperature field and it is subsequently employed as input to calculate the deformation field. To calculate large and permanent deformations, the static structural mode of ANSYS was utilized combined with the large deflection mode (nonlinear large deformations). Therefore, the transition from the elastic regime to the plastic regime can be calculated and the permanent large deformation of the glass substrate can be obtained. The substrate is considered fixed at the edges. The simulations are performed for three different scanning speeds. The scanning speeds were 4.61 W with 75 mm/s, and 10 W with 1 m/s and 1.25 m/s, respectively. The simulation results are presented in Fig. 5 and Fig. 6, showing that for all cases, the maximum deformation is 100 nm for scanning speed 75 mm/s. However, as it will be shown later, to inquire whether this permanent deformation can be considered viable for the recrystallized thin film, the simulations were compared with the experimental measurements.

3. Results and discussions

The crystallization mechanism at each zone is investigated from the scope of both experiments and simulations. Considering the length of beam (~ 290 μm) as marked in Fig 1.**B**, zone 1 is mainly heated by transverse heat conduction from zone 2. Zone 1 (fine grains) is fully melted from solid to liquid after its temperature reaches the melting point (~1420 K) of a-Si. Nevertheless, it is quenched quickly due to the heat loss to the substrate so this regime consists of fine grains (~ 90 nm), delineated in Fig. 3**A**-3**ii**, with a narrow transition between a-Si and p-Si. Fig. 4**A** shows the Raman spectroscopy measurements (Renishaw), captured for the boundary from the a-Si to zone 1 with 1 μm resolution (i.e., marked from Area 'A' to 'D'). For the a-Si, the Raman spectrum indicates the density of the states of the transverse optical phonon (TO) mode centered at 480 cm^{-1} with a broad width. It begins revealing the characteristics of p-Si Raman spectrum (peak at 514.6 cm^{-1} and full width at half maximum (FWHM) equal to 16.4 cm^{-1}) as the Raman probe laser is scanned towards zone 1. However, as the diameter of Raman laser beam utilizing the Olympus MS Plan 100X (NA = 0.95) lens is less than 1 μm and this regime ends within 4 ~ 5 μm, a-Si and p-Si are coalesced within this regime as partial melting [21]. Hence, the p-Si and a-Si Raman spectra are consistent with the simulation result presented in Fig. 2**E**, which predicted the partial melting zone width to be approximately equal to 5 μm. At the center of

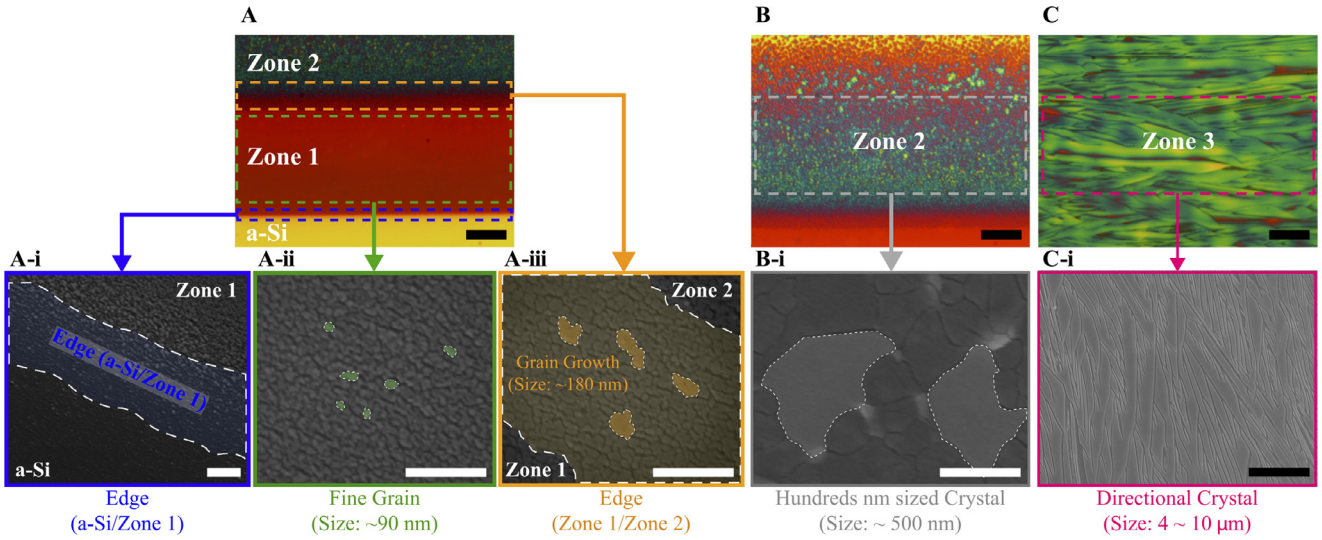

Fig. 3. Secco-etched optical microscope images (A) from a-Si to zone 2, (B) the center of zone 2, and (C) the center of zone 3. **SEM images** (A-i) for the edge between a-Si and zone 1, (A-ii) the center of zone 1, which shows fine grains with 90 nm, and (A-iii) the edge between zone 1 and zone 2 consisting of ~180 nm grains. (B-i) Nano-poly crystals with size approximately equal to 500 nm at the center of zone 2. (C-i) laterally grown crystals at the center of zone 3. The black scale bar is 10 μm, and the white scale bar is 500 nm.

zone 1, the Raman spectrum (514.6 cm^{-1}) of p-Si in this area becomes close to that of p-Si (~ 517.8 cm^{-1}) in zone 2. Similar analysis of the boundary between zone 1 and zone 2 is applied, presented in **Fig. 3A-3iii**, and the respective Raman spectra are presented in **Fig. 4B**. Within 7 μm (from Area 'A' to 'F'), the Raman frequency is shifted from 517.8 cm^{-1} and FWHM 8 cm^{-1} to 518.9 cm^{-1} and FWHM 6 cm^{-1}, which reveals that high quality of p-Si film is initiated at zone 2. Zone 2 (~ 500 nm sized crystals (**Fig. 3A-3iii**) to **(3B-i)**, is affected by higher heating than zone 1 due to absorption of the laser source, while the simulation results shown in **Fig 2C** verify that a-Si in zone 2 is fully melted into L-Si, but heated below the equilibrium c-Si melting point of 1685 K. However, for excimer laser annealing (ELA), heating close to 1685 K results in 100 ~ 150 nm sized grains [1]. The incongruity between the BLA and the ELA may originate from the different quench rates, and the cooling durations [22]. BLA has a slower quench rate (~ 10^8 K/s based on our numerical simulation) induced by the presence of heated SiO_2 layer due to its large thermal diffusion length. Hence, the preheated SiO_2 layer acts as a thermal buffer layer, so it precipitates a much longer time for nuclei to grow and propagate in the size scale of hundreds of nanometers under 1685 K compared to the cooling duration of tens of nanoseconds for the excimer laser annealing [1]. Therefore, L-Si is transformed into hundreds of nanometers or even a few microns poly crystallites with increasing size towards the center. However, the nanoseconds duration single shot of ELA, combined with the skin depth absorption at high laser fluences (i.e., complete melting regime) causes a rapid quenching by heat conduction to the substrate. Hence, lateral growth is hindered in such a short cooling duration (~ 10^{10} K/s), due to the vertical grain growth [4]. As it is predicted by the simulations (**Fig. 2B and 2C**), zone 3 is primarily heated by the high fluence of laser with hundreds of microseconds annealing duration (380 μs at 75 mm/s), resulting in superheating above the equilibrium melting point 1685 K at the center regime. Combined with the heated thermal buffer layer, the corollary of this additional heating process allows a prolonged cooling rate eliminating the possibility of spontaneous nucleation, consistent with the directional crystal growth requirement [5]. The crystal grains then elongate along the scanning direction (**Fig. 3C and 3C-i**) conducive by the solidification in the back edge of the melt pool, whose width was calculated approximately equal to 45 μm (**Fig. 2B**).

Raman spectroscopy is further employed to investigate the crystallinity of p-Si at zone 2 and zone 3 at 10 arbitrary points of each zone. **Fig. 4C** shows that the Raman scattering intensity of zone 2 is enhanced compared to that of zone 3 by a factor of 2.3 for the same intensity of the incident Raman laser beam. It is revealed that the beam scattering

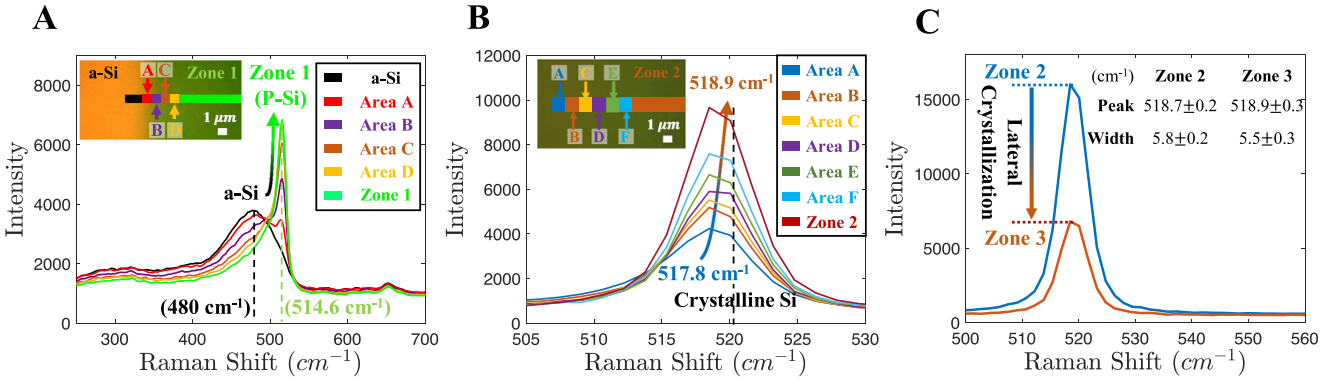

Fig. 4. Raman spectroscopy with 1 μm resolution **for laser irradiation conditions at 4.61 W and 75 mm/s** (A) partial melting regime exists within 5 μm between a-Si and zone 1, (B) boundary between zone 1 and zone 2. (C) Raman signal intensity of zone 2 is enhanced by a factor of 2.3 than that of zone 3 due to the SERS effect originating from the spherical shapes of zone 2. 10 random points of Raman spectra are summarized at each zone in inset of (C), indicating high quality of p-Si with low tensile stress.

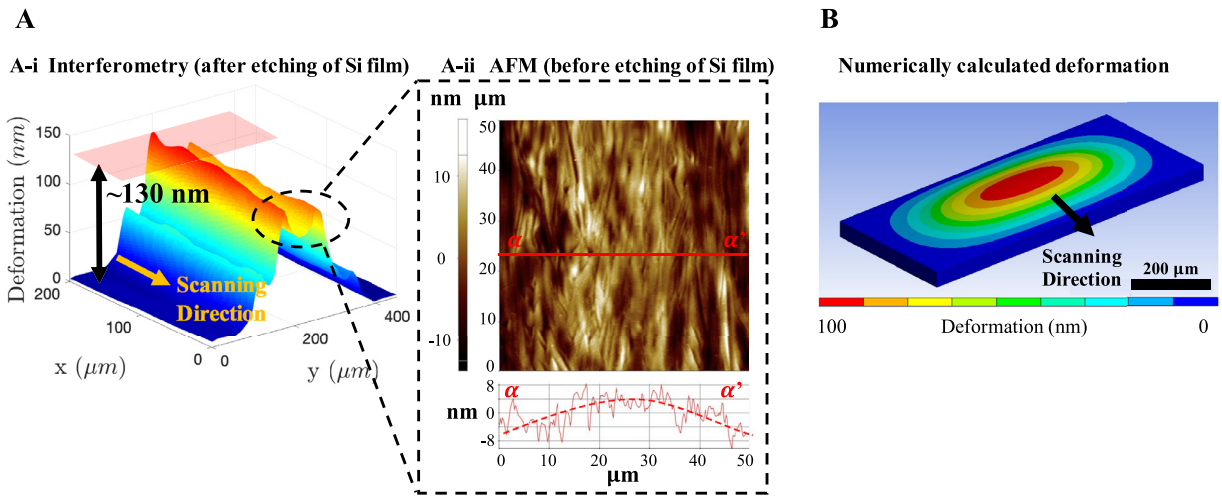

Fig. 5. Glass deformation profiles (A) Interferometer measurement of 4.61 W with 75 mm/s. The measurement shows that the maximum deformation height is 130 nm and the formation of two convex morphologies. (B) The calculated deformation field for the same laser irradiation conditions, with 100 nm maximum deformation height.

by the nano-crystallites at zone 2 is greater than the crystalline silicon at zone 3. The reason is that the magnetic response of the incident laser beam (532 nm), by resonant Raman scattering, is bolstered when the size of the diameter is at hundreds of nanometers. [23]. Moreover, the density of states at the TO mode at zone 2 and zone 3 is centered at 518.9 cm^{-1} with FWHM equal to 5.7 cm^{-1} depicted **Fig. 3C**, approaching the peak of the single crystalline Si (c-Si) wafer (520.2 ± 0.5 cm^{-1} with 4.6 cm^{-1} FWHM) [24]. Down-shifting of the phonon peaks was applied to measure the residual tensile stress of p-Si film after the annealing process [25]. Compared to the density of the TO modes at 514 ~ 517 cm^{-1} achieved by ELA [26], BLA attains remarkably lower deviation from the Raman frequency of c-Si. A potential explanation for this finding could be the prolonged volumetric melting and cooling of a single thin film element without an impurity element. This provides an epitaxial solidification mechanism through the entire film thickness within the grain. Hence, the same lattice structure and orientation within the grain [22] can be obtained due to the lattice mismatching of a semi-coherent interface between p-Si film and SiO_2 layer. Based on the aforementioned Raman spectroscopy results, the deviation of the Raman shift of p-Si from c-Si is 1.3 cm^{-1}, and the corresponding stress inside the film is expected to be in the order of magnitude of 565 MPa [27]. To juxtapose the reported result with the simulations, 3D elasticity coupled thermal expansion must be employed. The normal stress can be calculated by the following equation [28],

$$\sigma_{ij} = \frac{E}{(1+\nu)}\varepsilon_{ij} + \frac{E\nu}{(1-2\nu)(1+\nu)}\varepsilon_{\kappa\kappa}\delta_{ij} - \frac{E}{(1-2\nu)}a\Delta\Theta\delta_{ij} \quad (1)$$

Where *i, j* correspond to the coordinate system directions, $\varepsilon_{\kappa\kappa}$ is the trace of the strain tensor, $\Delta\Theta$ corresponds to the temperature difference from

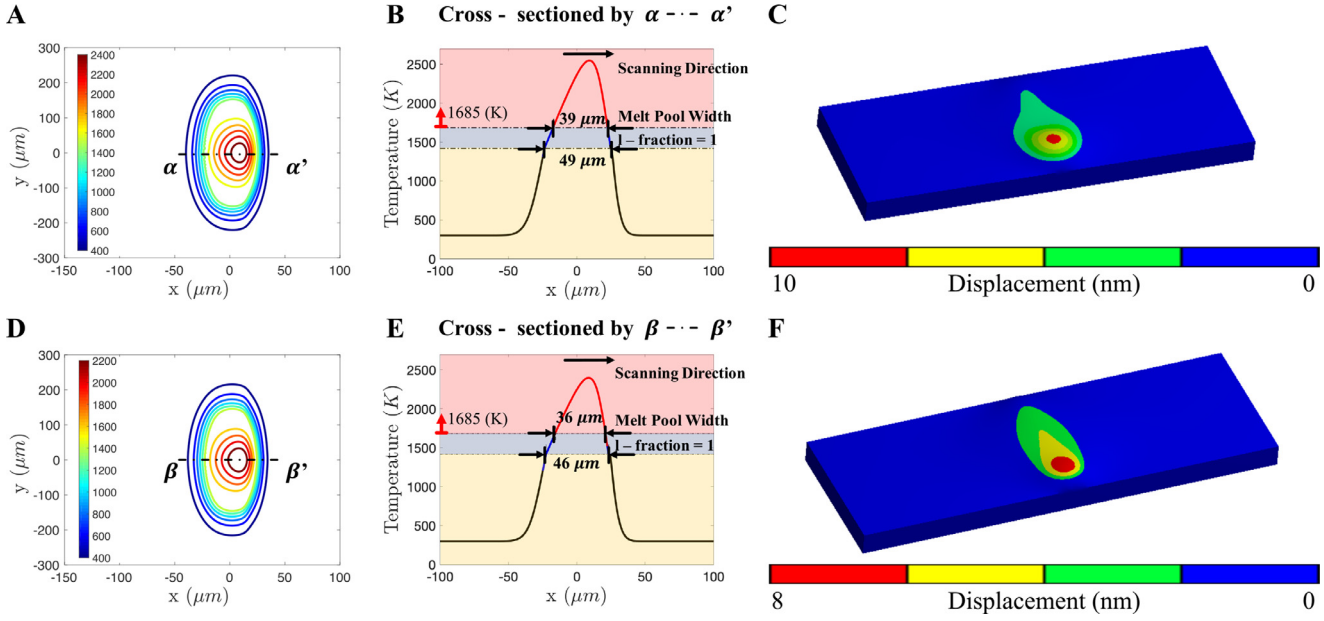

Fig. 6. Simulation results of optimized laser power and scanning speeds: 10 W with 1 m/s (A) isotherms, (B) melt pool width (39 μm) > 10 μm, and (C) calculated deformation height ~ 30 nm. **10 W with 1.25 m/s** (D) isotherms, (E) melt pool (36 μm) > 10 μm, and (F) deformation height will be 10 nm under. + ***x*** and the white arrow indicate the scanning direction. It must be noted that as the laser process becomes faster, the deformation becomes less symmetric because the heat flux becomes transient and it is not uniform as the laser beam passes through a specific path.

displacement equal to 0 to the maximum displacement, δ_{ij} corresponds to the Kronecker's delta, α is the linear thermal expansion coefficient and E, ν are the Young's Modulus and Poisson ratio, respectively. The modulus of elasticity and the Poisson ratio for Silicon are approximately equal to 130 GPa and 0.22, respectively. The thermal expansion coefficient can be estimated to be $10^{-6}\ K^{-1}$ [29], while the temperature difference is provided in **Fig. 2B**. Assuming that the deformation in the lateral direction is much higher than in the other directions and for elongation equal to 100 nm, Eq. (1) gives normal stress of magnitude equal to 572 MPa having 1.2% divergence from the experimental result. Hence, the numerical simulation is consistent regarding the estimation of the stresses.

The heat flux calculated from the temperature field is used to obtain the thermal deformation. After etching the p-Si film by a silicon etchant (33% deionized water / 3% NH_4F / 64% HNO_3), the permanent deformation profile is measured by a Zygo interferometer, having the maximum value of 130 nm at the center (**Fig. 5A-i**). The calculated deformation height from the finite element analysis was 100 nm (**Fig. 5B**), which is consistent with the measured result. A potential reason for their difference is that there is more significant variance in the thermal expansion coefficient of the glass at such high temperatures [29]. Precise measurements of the thermal expansion coefficient at this temperature regime could diminish this difference. However, compared to the simulation results, the morphology in **Fig. 5A** has two bumped formations. Considering the center regime at zone 3 measured by an Atomic Force Microscopy (**Fig. 5A-ii**) before etching of Si film, these bumps are not observed, but instead a symmetric volume gain at the center has been identified. Therefore, it is inferred that these bumps are resulted from the etching of PECVD SiO_2 layer by the ammonium fluoride [30].

Therefore, faster scanning speed must be utilized to minimize the thermal damage on the substrate. Nevertheless, for the same laser irradiation distribution the melt pool width will be smaller at higher scanning speeds, whereas the temperature drop at the crystallization interface will be faster. Thus, the final objective is to achieve a deformation profile comparable to the roughness of the p-Si film (average roughness of zone 2 is 3.8 nm, and that of zone 3 is 2.6 nm, not presented here), while maintaining a melt width of more than 10 μm above 1685 K where superheating process occurs, to support the directional crystal growth. To comprehend how faster scanning speeds will affect the glass substrate deformation, finite element analysis is also performed for each case. More specifically, the thermal diffusion length is expected to be approximately equal to 20 μm at 4.61 W with 75 mm/s. Repeating the modeling for higher scanning speeds, such as 1 m/s and 1.25 m/s, the thermal diffusion lengths are 5.3 μm and 4.7 μm, respectively. Performing the heat conduction equation simulations again with 10 W, 11 W, 12 W, and 13 W for the above scanning speeds, revealed that the laser processing conditions with 10 W at 1 m/s and 1.25 m/s are the optimum ones. The calculated deformation fields presented at **Fig. 6C and 6F** show the deformation profile of the substrate for 10 W and scanning speed 1 m/s and 1.25 m/s. The maximum deformation for both cases is 10 nm and 8 nm respectively. Compared to the first case (i.e. 75 mm/s), for these cases it is observed that the deformation peak is shifted with respect to the center of the laser beam, as a consequence of transient effects of the heat flux. Therefore, the time variance of the heat flux in different zones of the substrate distorts the symmetrical profile of slow scanning speed. The corollary is a permanent deformation along the path of the laser beam, until the edge is reached and the permanent deformation has a peak region, as it was observed in **Fig. 5B**. For lower speed (75 mm/s), the heat flux profile is nearly symmetric with respect to a Cartesian coordinate system fixed at the center of the substrate. For the first case, because of the low speed of the laser beam, the structural analysis can be performed as static, however, for higher speeds, quasi-transient structural analysis must be utilized, as the heat flux profile will vary in amplitude as a function of time. Both the thermal analysis and the structural analysis are congruous with the experiments, regarding the transition regime between a-Si and p-Si, and the glass thermal deformation height. Nevertheless, the scanning speed of the laser beam affects the surface tension of silicon during the melting. Subsequently, the shear stresses that are developed to keep attached the silicon film and the glass substrate will vary. To improve the modeling of the system regarding the shear effects, the fluidic effects of the material can be included. However, this will increase the complexity of the model and methods to mitigate the computational cost and obtain results closer to the experimental ones are under the scope of future research. The expected deformation profiles are comparable to the roughness of p-Si film (~ 5 nm), and therefore the deformation regime for both cases is conducive for a functional device. Hence, these results crucially indicate that the BLA process can achieve high quality p-Si thin film with highly suppressed thermal deformation.

4. Conclusions

To investigate physical mechanisms associated with the BLA process, we analyzed the phase transformation mechanisms of a-Si and the glass texturing by heat conduction performing experiments and numerical simulations. It was observed that volumetric heating dominates the melting process of a-Si because of the longer optical penetration depth (22 nm at $\lambda = 440$ nm) and longer heat diffusion length by the BLA. Large grained crystals, ranging from hundreds of nanometers grains to 4 μm × 10 μm directional crystals, were fabricated and observed by optical and electron microscopy. Raman spectroscopy of the p-Si thin film showed the high crystallinity having limited residual stresses inside the film. Finally, thermal analysis of the glass substrate verified that fast scanning speed (1 m/s ~ 1.25 m/s) with 10 W will efficiently suppress the thermal damage of the glass substrate and the deformation of the glass substrate is comparable to the roughness of p-Si. Our findings reveal that BLA can be utilized for crystallization of a-Si film on glass substrate by suppressing the thermal deformation and unravel the mechanisms governing the controlled crystal growth. This comprehensive analysis, encompassing both experiments and thermo-mechanical simulations, provides the modeling and experimental procedures that need to be addressed, regarding the utility of BLA for the next generation LTPS applications.

CRediT authorship contribution statement

Minok Park: Conceptualization, Writing - original draft, Writing - review & editing. **Zacharias Vangelatos:** Formal analysis, Writing - original draft, Writing - review & editing. **Yoonsoo Rho:** Formal analysis, Writing - review & editing. **H.K. Park:** Resources, Writing - review & editing. **Jin Jang:** Resources, Writing - review & editing. **Costas P Grigoropoulos:** Supervision, Writing - review & editing.

Conflict of Interest

We confirm that this manuscript has not been submitted to any other journals. All authors agree with the submission to *Thin Solid Films*. Additionally, the authors have no conflicts of interest to disclose. Thank you for your consideration of our manuscript. We look forward to hearing from you.

Acknowledgements

The work conducted at UCB's Laser Thermal Laboratory was partially supported by the NSF under the grant CMMI-1363392. The authors also acknowledge the help of Ron Synowicki of J.A. Woollam Co. for the ellipsometric measurement of optical properties, and access to the interferometer by Dayana Oropeza in Lawrence Berkeley National Laboratory. Moreover, the authors thank Youngkyu Kim and Dayeol Lee for their feedback during discussions, and Letian Wang and Hwansung

Choe for assisting with the selection of the required chemicals.

References

[1] M. Hatano, S. Moon, M. Lee, K. Suzuki, C.P. Grigoropoulos, Excimer laser-induced temperature field in melting and resolidification of silicon thin films, J. Appl. Phys 87 (2000) 36, https://doi.org/10.1063/1.371823.

[2] M. Lee, S. Moon, M. Hatano, K. Suzuki, C.P. Grigoropoulos, Relationship between fluence gradient and lateral grain growth in spatially controlled excimer laser crystallization of amorphous silicon films, J. Appl. Phys 88 (2000) 4994, https://doi.org/10.1063/1.1314303.

[3] C.H. Chou, I.C. Lee, P.Y. Yang, M.J. Hu, C.L. Wang, C.Y. Wu, Y.S. Chien, K.Y. Wang, H.C. Cheng, Effects of crystallization mechanism on the electrical characteristics of green continuous-wave-laser-crystallized polycrystalline silicon thin film transistors, Appl. Phys. Lett 103 (2013) 053515, , https://doi.org/10.1063/1.4812669.

[4] K. Morikawa, T. Okamoto, T. Kojima, S. Yura, J. Nishimae, Y. Sato, M. Tanaka, M. Inoue, H. Nagata, 33.3: comparison of poly-si tft characteristics crystallized by a YAG2ω laser and an excimer laser, SID Symposia Digest of Technical Papers 35 (2005) 1088–1091, https://doi.org/10.1889/1.1821319.

[5] L. Xu, C.P. Grigoropoulos, T.J. King, High-performance thin-silicon-film transistors fabricated by double laser crystallization, J. Appl. Phys. 99 (2006) 034508, , https://doi.org/10.1063/1.2171807.

[6] S. Jin, Y. Choe, S. Lee, T.W. Kim, M. Mativenga, J. Jang, Lateral grain growth of amorphous silicon films with wide thickness range by blue laser annealing and application to high performance poly-Si TFTs, IEEE Electron Device Lett 37 (2016) 291–294, https://doi.org/10.1109/LED.2016.2518705.

[7] S. Jin, S. Hong, M. Mativenga, B. Kim, H.H. Shin, J.K. Park, T.W. Kim, J. Jang, Low temperature polycrystalline silicon with single orientation on glass by blue laser annealing, Thin Solid Films 616 (2016) 838–841, https://doi.org/10.1016/j.tsf.2016.10.026.

[8] T. Noguchi, Y. Chen, T. Miyahira, J. De Dieu Mugiraneza, Y. Ogino, Y. Iida, E. Sahota, M. Terao, Advanced micro-polycrystalline silicon films formed by blue-multi-laser- diode annealing, Jpn. J. Appl. Phys 49 (2010), https://doi.org/10.1143/JJAP.49.O3CA1O 03CA10.

[9] K. Shirai, T. Noguchi, Y. Ogino, E. Sahota, Opto-thermal analysis of blue multi laser diode annealing (BLDA), IEICE Trans. Electron E93.C (2010) 1499–1503, https://doi.org/10.1587/transele.e93.c.1499.

[10] T. Okada, J. De Dieu Mugiraneza, K. Shirai, T. Suzuki, T. Noguchi, H. Matsushima, T. Hashimoto, Y. Ogino, E. Sahota, Crystallization of si thin film on flexible plastic substrate by blue multi-laser diode annealing, Jpn. J. Appl. Phys 51 (2012), https://doi.org/10.1143/JJAP.51.03CA02 03CA02.

[11] Y.H. Jung, S. Hong, S. Lee, S. Jin, T.-.W. Kim, Y. Chang, J. Jang, Sequential lateral crystallization of amorphous silicon on glass by blue lase annealing for high mobility thin-film transistors, Thin Solid Films 681 (2019) 93–97, https://doi.org/10.1016/j.tsf.2019.04.023.

[12] S.G. Ryu, I. Gruber, C.P. Grigoropoulos, D. Poulikakos, S.J. Moon, Large area crystallization of amorphous si with overlapping high repetition rate laser pulses, Thin Solid Films 520 (2012) 6724–6729, https://doi.org/10.1016/j.tsf.2012.07.052.

[13] F. Secco d'Aragona, Dislocation etch for (100) planes in silicon, J. Electrochem. Soc. 119 (1972) 948–951, https://doi.org/10.1149/1.2404374.

[14] H.C. Webber, A.G. Cullis, N.G. Chew, Computer simulation of high speed melting of amorphous silicon, Appl. Phys. Lett 43 (1983) 669, https://doi.org/10.1063/1.94440.

[15] S. de Unamuno, E. Fogarassy, A thermal description of the melting of c- and a-silicon under pulsed excimer lasers, Appl. Surf. Sci 36 (1989) 1–11, https://doi.org/10.1016/0169-4332(89)90894-5.

[16] K. Higuchi, K. Kimura, A. Mizuno, M. Watanabe, Y. Katayama, K. Kuribayashi, Density and structure of undercooled molten silicon using synchrotron radiation combined with an electromagnetic levitation technique, J. Non. Cryst. Solids. 353 (2007) 2997–2999, https://doi.org/10.1016/j.jnoncrysol.2007.05.029.

[17] H. Kobatake, H. Fukuyama, T. Tsukada, S. Awaji, Noncontact modulated laser calorimetry in a dc magnetic field for stable and supercooled liquid silicon, Meas. Sci. Technol 21 (2010) 025901, , https://doi.org/10.1088/0957-0233/21/2/025901.

[18] S.M. Lee, D.G. Cahill, Heat transport in thin dielectric films, J. Appl. Phys. 81 (1997) 2590, https://doi.org/10.1063/1.363923.

[19] C.P. Grigoropoulos, R.H. Buckholz, G.A. Domoto, A thermal instability in the laser-driven melting and recrystallization of thin silicon films on glass substrates, J. Heat Transfer 109 (1987) 841–847, https://doi.org/10.1115/1.3248192.

[20] J. Arndt, F. Häberle, Thermal expansion and glass transition temperatures of synthetic glasses of plagioclase-like compositions, contrib. to mineral, Petrol 39 (1973) 175–183, https://doi.org/10.1007/BF00375739.

[21] G. Kanellis, J.F. Morhange, M. Balkanski, Effect of dimensions on the vibrational frequencies of thin slabs of silicon, Phys. Rev. B 21 (1980) 1543–1548, https://doi.org/10.1103/PhysRevB.21.1543.

[22] D.A. Porter, K.E. Easterling, M.Y.A. Sherif, Phase transformations in metals and alloys, third edition, CRC Press, 2009.

[23] P.A. Dmitriev, D.G. Baranov, V.A. Milichko, S.V. Makarov, I.S. Mukhin, A.K. Samusev, A.E. Krasnok, P.A. Belov, Y.S. Kivshar, Resonant raman scattering from silicon nanoparticles enhanced by magnetic response, Nanoscale 8 (2016) 9721–9726, https://doi.org/10.1039/c5nr07965a.

[24] J.H. Parker, D.W. Feldman, M. Ashkin, Raman scattering by silicon and germanium, Phys. Rev 155 (1967) 712–714, https://doi.org/10.1103/PhysRev.155.712.

[25] S. Nakashima, Y. Inoue, M. Miyauchi, A. Mitsuishi, T. Nishimura, T. Fukumoto, Y. Akasaka, Raman microprobe study of recrystallization in ion-implanted and laser-annealed polycrystalline silicon, J. Appl. Phys. 54 (1983) 2611, https://doi.org/10.1063/1.332334.

[26] C.C. Kuo, Micro-Raman spectroscopy characterization of polycrystalline silicon films fabricated by excimer laser crystallization, Opt. Lasers Eng 47 (2009) 612–616, https://doi.org/10.1016/j.optlaseng.2008.06.018.

[27] I. De Wolf, Stress measurements in si microelectronics devices using Raman spectroscopy, J. Raman Spectrosc. 30 (1999) 877–883 10.1002/(sici)1097-4555(199910)30:10<877::aid-jrs464>3.3.co;2-x.

[28] M. Gurtin, The linear theory of elasticity, Springer-Verlag (1972).

[29] Y. Okada, Y. Tokumaru, Precise determination of lattice parameter and thermal expansion coefficient of silicon between 300 and 1500 K, J. Appl. Phys. 56 (1984) 314–320, https://doi.org/10.1063/1.333965.

[30] K. Osseo-Asare, Etching kinetics of silicon dioxide in aqueous fluoride solutions: a surface complexation model, J. Electrochem. Soc. 143 (2006) 1339–1347, https://doi.org/10.1149/1.1836640.